



MIT Open Access Articles

Photo-excitation Cascade and Multiple Carrier Generation in Graphene

The MIT Faculty has made this article openly available. **Please share** how this access benefits you. Your story matters.

Citation	Tielrooij, K. J., J. C. W. Song, S. A. Jensen, A. Centeno, A. Pesquera, A. Zurutuza Elorza, M. Bonn, L. S. Levitov, and F. H. L. Koppens. "Photoexcitation Cascade and Multiple Hot-Carrier Generation in Graphene." Nat Phys 9, no. 4 (February 24, 2013): 248–252.
As Published	http://dx.doi.org/10.1038/nphys2564
Publisher	Nature Publishing Group
Version	Author's final manuscript
Citable link	http://hdl.handle.net/1721.1/88511
Terms of Use	Article is made available in accordance with the publisher's policy and may be subject to US copyright law. Please refer to the publisher's site for terms of use.

Photo-excitation Cascade and Multiple Carrier Generation in Graphene

K.J. Tielrooij,^{1,*} J.C.W. Song,^{2,3} S.A. Jensen,^{4,5} A. Centeno,⁶ A. Pesquera,⁶
A. Zurutuza Elorza,⁶ M. Bonn,⁴ L.S. Levitov,² and F.H.L. Koppens^{1,*}

¹*ICFO - Institut de Ciències Fotòniques, Mediterranean Technology Park, Castelldefels (Barcelona) 08860, Spain*

²*Department of Physics, Massachusetts Institute of Technology, Cambridge, Massachusetts 02139, USA*

³*School of Engineering and Applied Sciences, Harvard University, Cambridge, Massachusetts 02138, USA*

⁴*Max Planck Institute for Polymer Research, Ackermannweg 10, 55128 Mainz, Germany*

⁵*FOM Institute AMOLF, Amsterdam, Science Park 104, 1098 XG Amsterdam, Netherlands*

⁶*Graphenea SA, 20018 Donostia-San Sebastián, Spain*

The conversion of light into free electron-hole pairs constitutes the key process in the fields of photodetection and photovoltaics. The efficiency of this process depends on the competition of different relaxation pathways and can be greatly enhanced when photoexcited carriers do not lose energy as heat, but instead transfer their excess energy into the production of additional electron-hole pairs via carrier-carrier scattering processes. Here we use Optical pump - Terahertz probe measurements to show that in graphene carrier-carrier scattering is unprecedentedly efficient and dominates the ultrafast energy relaxation of photoexcited carriers, prevailing over optical phonon emission in a wide range of photon wavelengths. Our results indicate that this leads to the production of secondary hot electrons, originating from the conduction band. Since hot electrons in graphene can drive currents, multiple hot carrier generation makes graphene a promising material for highly efficient broadband extraction of light energy into electronic degrees of freedom, enabling high-efficiency optoelectronic applications.

I. MAIN TEXT

For many optoelectronic applications, it is highly desirable to identify materials in which an absorbed photon is efficiently converted to electronic excitations. The unique properties of graphene, such as its gapless band structure, flat absorption spectrum [1] and strong electron-electron interactions [2], make it a highly promising material for efficient broadband photon-electron conversion [3]. Indeed, recent theoretical work has anticipated that in graphene multiple electron-hole pairs can be created from a single absorbed photon during energy relaxation of the primary photoexcited e-h pair [4, 5]. A photo-excited carrier relaxes initially through two competing pathways: carrier-carrier scattering and optical phonon emission. In the former process the energy of photoexcited carriers remains in the electron system, being transferred to secondary electrons that gain energy (become hot), whereas in the phonon emission process the energy is lost to the lattice as heat. While recent experiments have shown that photoexcitation of graphene can generate hot carriers [6, 7], it remains unknown how efficient this process is with respect to optical phonon emission.

Here we study the energy relaxation process of the primary photoexcited e-h pair in doped single-layer graphene. In particular, we quantify the branching ratio between the two competing relaxation pathways. Given the challenging timescale with which these processes occur, we employ an ultrafast Optical pump - Terahertz (THz) probe measurement technique, where we exploit the variation of the photon energy of the pump light. Changing this photon energy is crucial as it allows us to prepare the system with photoexcited carriers having a prescribed initial energy determined by the photon energy, and follow the ensuing energy relaxation dynamics. We show experimentally, in combination with theoretical modeling, that carrier-carrier scattering is the dominant relaxation process. This process leads to the creation of secondary hot electrons that originate from the conduction band.

We note that assigning a ‘conventional name’ to a process in which secondary hot carriers are generated by photoexcited carriers in graphene, is by no means a trivial matter. This is so because somewhat different nomenclature is used in the optical studies of semiconductors and metals: electrons and holes in semiconductors are defined with respect to the conduction and valence bands, whereas in metals the distinction between the states above and below the Fermi level plays the key role. Doped graphene can be viewed as a mixture of both: it is a semimetal with the Fermi level detuned away from the Dirac point. To minimize confusion, and at the same time to make

*Correspondence to: klaas-jan.tielrooij@icfo.es, frank.koppens@icfo.es

the discussion of our results unambiguous, we will denote the process in question as “hot-carrier multiplication.” This *intraband* process is different from conventional carrier multiplication observed in semiconductor systems [8–11] and theoretically predicted for undoped graphene [4, 5], where additional e-h pairs originate from *interband* transitions. However, the generation of secondary hot carriers from the conduction band in doped graphene is a technologically relevant relaxation process since the thermoelectric effect dominates the optoelectronic response of graphene [6, 7]. For hot carrier multiplication, the total number of carriers in the conduction band does not change due to carrier-carrier scattering. However, the number of hot carriers (i.e. carriers with an energy above the Fermi level) increases. It is via this multiplication of hot electrons in the conduction band that the energy of the primary photoexcited carrier is “harvested” by the electron subsystem and later used to generate an optoelectronic response.

The employed technique consists of an ultrafast optical pump pulse that excites carriers and a THz probe pulse that passes through the sample after a variable delay time. The THz pulses afford an exquisite time-resolved probe of the high frequency photoconductive response of photoexcited carriers, as reviewed in Ref. [12]. This technique has been used before with a fixed pump wavelength to study charge dynamics in multilayer graphene [13–18], and with a variable pump wavelength to study the effects of carrier-carrier interaction in semiconductor materials [8, 9, 11]. Here we apply this technique with variable pump wavelength to examine the energy relaxation cascade of photoexcited carriers in graphene. We use a monolayer of intrinsically doped graphene, in contrast to previous optical pump - THz probe studies which used multilayer (undoped) graphene [13–18]. We find that the photoexcited density of carriers with energy above the Fermi energy scales linearly with photon energy (for constant absorbed photon density). This scaling is found over a wide range that spans almost an order of magnitude in photon wavelength. Our experimentally observed linear scaling indicates that carrier-carrier scattering is remarkably efficient, in excellent agreement with our results from a theoretical model that considers electron-electron scattering and electron-optical phonon scattering.

The intrinsically doped graphene sample that we use for our study consists of a monolayer of CVD graphene transferred onto a quartz substrate. From Raman spectroscopy we estimate a Fermi energy of $\mu \sim 0.17 \pm 0.05$ eV, which corresponds to an intrinsic carrier concentration of $\sim 2 \times 10^{12}$ carriers/cm². We further characterize the sample using THz transmission (without optical excitation) and find that the graphene monolayer has a spectrally flat absorption of $\sim 5\%$ in the 0.4–1.6 THz region. This absorption is due to intraband momentum scattering of the intrinsic carriers (Drude conductivity) with an extracted average transport time of $\tau_{\text{tr}} \sim 20$ fs (see supplementary online material for a detailed sample characterization).

Our method for probing the energy relaxation dynamics of photoexcited carriers is illustrated in Fig. 1a. We optically excite the graphene/quartz stack and examine the pump-induced change in THz transmission $\Delta T = T - T_0$, where T and T_0 are the transmission with and without photoexcitation, respectively. The THz pulses follow the pump pulses after a tunable time delay with a time resolution of ~ 100 fs. Because the graphene layer is thin, the change in transmission is directly related to the photoconductive response so that $\frac{\Delta T}{T_0} \propto -\Delta\sigma$ (see supplementary online material). Here $\Delta\sigma$ is the pump-induced change in the THz conductivity, which we refer to as the THz photoconductivity.

The essential features of the observed dynamics are exemplified by two typical differential transmission time traces shown in Fig. 1b. The observed temporal evolution is non-monotonic: the differential transmission first rises in an approximately linear fashion, reaching a peak at a delay time $\tau_{\text{peak}} \sim 200$ fs, and finally decays on a longer timescale ~ 1.4 ps. These observations can be explained as follows. During the initial rise, $t \lesssim \tau_{\text{peak}}$, carrier-carrier scattering between the photoexcited carriers and the carriers in the Fermi sea promotes carriers from below to above the Fermi level (see middle inset of Fig. 1b). Thus the effective temperature of the carrier distribution increases, peaking at $t \approx \tau_{\text{peak}}$ when the photoexcited carriers have relaxed and a hot carrier distribution is established. Subsequent relaxation occurs due to electron-lattice cooling, which is a relatively slow process with a characteristic timescale (~ 1.4 ps) much greater than τ_{peak} . These dynamics are very similar to those observed in earlier optical pump-THz probe studies on multilayer (undoped) graphene [13–18].

The measured change in transmission $\frac{\Delta T}{T_0}$ is positive, meaning that the conductivity is reduced as a result of photoexcitation, $\Delta\sigma < 0$. The observation of negative photoconductivity is in agreement with recent THz pump-probe studies on monolayer graphene [19, 20]. The reduction in conductivity is naturally related to secondary hot carrier excitation processes: Since the momentum scattering time $\tau_{\text{tr}}(\epsilon)$ increases with carrier energy ϵ [21–23], the creation of a hot carrier distribution after photoexcitation leads to a change in the real part of conductivity that has a negative sign (see supplementary online text). In contrast, for multilayer (undoped) graphene a positive change in the conductivity was observed, because in that case photoexcitation leads to additional e-h pairs in the conduction band [13–18].

Key insight into the processes contributing to the energy relaxation cascade comes from examining how the differential transmission signal $\frac{\Delta T}{T_0}$ peak value scales with the photon energy hf , which in our experiment is varied over a wide range, from the infrared (0.16 eV) to the ultraviolet (4.65 eV). Since the initial photoexcited carrier energy, $\epsilon_i = \frac{1}{2}hf$, determines where the cascade begins, we can track how the photoexcited carriers relax at each stage of the energy re-distribution process. As a first step, we analyze the peak value $\frac{\Delta T}{T_0}$ dependence on absorbed photon density N_{photon} (i.e. the number of absorbed photons per unit of area), which is displayed in Fig. 1c, for six different photon wavelengths. In the fluence regime employed here, the signal increases linearly with absorbed photon density for each photon energy. The linear dependence of THz photoconductivity on fluence at fixed photon energy indicates that in this regime each photoexcited carrier acts independently from the other photoexcited carriers.

Proceeding with the analysis we observe that increasing the photon energy at a *fixed absorbed photon density* leads to a larger differential transmission signal at the peak. This is clear from the slopes in Fig. 1c that increase with photon energy. The origin of the increased signal for increased photon energy (at fixed absorbed photon density) is shown schematically in Fig. 1d. Here, increasing the photon energy leads to an increased number of electron-electron scattering events during the relaxation cascade and thus a hotter carrier distribution. In Fig. 2a we show the effect of increasing the photon energy by plotting the peak differential transmission signal normalized by absorbed photon density. Notably, the normalized signal scales approximately linearly with the photon energy, whereas energy relaxation through phonon emission would lead to a normalized signal that would be independent of photon energy.

It is instructive to combine these observations in a unified picture which provides an intuitive “bird’s eye view” of the energy relaxation cascade. We do this by plotting the interpolated experimental contours for the $\Delta T/T_0$ peak value as a function of photon energy and photon number (see Fig. 2d). Strikingly, the contours of constant $\Delta T/T_0$ bunch up at high photon energy and spread out at low photon energy. This confirms that the two ways to achieve a hotter distribution of carriers – either by increasing the absorbed photon density or by increasing the photon energy – are completely interchangeable. The hyperbolic shape also indicates that the differential transmission signal scales with the fluence (incident energy per area, $N_{\text{photon}} \times hf$). This constitutes a clear qualitative signature of the dominance of carrier-carrier scattering. Without carrier-carrier scattering, the magnitude of the response would be determined only by the absorbed photon density, and not the excitation energy; the contour lines would have been essentially vertical, with no change in $\Delta T/T_0$ as photon energy is varied (see also Fig. 2f). From these “bird’s eye view” plots we conclude that carrier-carrier scattering plays an important role in the energy relaxation cascade. Below we develop this notion more quantitatively and estimate the (energy dependent) efficiency of carrier-carrier scattering in graphene.

The efficiency of carrier-carrier scattering depends on the branching ratio between the two processes: (i) carrier-carrier scattering vs. (ii) electron-optical phonon scattering that occur during the rise stage, $0 < t \lesssim \tau_{\text{peak}}$. To extract this branching ratio, we develop a simple model for energy relaxation in the photoexcitation cascade and compare it with the data. The relaxation can be described in a general form via $d\epsilon/dt = -\mathcal{J}_{\text{el-el}}(\epsilon) - \mathcal{J}_{\text{el-ph}}(\epsilon)$, where ϵ is the photoexcited carrier energy and $\mathcal{J}_{\text{el-el}}$ and $\mathcal{J}_{\text{el-ph}}$ represent the energy relaxation rates for processes (i) and (ii). Our analysis relies on the fact that the characteristic time of the photoexcitation cascade starting at the photon energy $\epsilon = hf/2$ (at $t = 0$) and ending at the Fermi energy $\epsilon \approx \mu$ (at $t = \tau_{\text{peak}}$) is much longer than the carrier-carrier scattering time. Indeed, typical values $\tau_{\text{peak}} \sim 200$ fs measured in our experiment (see Fig. 1b) are considerably longer than the reported values for carrier-carrier scattering times, which are well below 100 fs [13, 24]. Thus the electron subsystem during the cascade can be described using an effective electron temperature which is distinct from the lattice temperature. Thermal equilibration with the lattice in graphene is slow [26–28], and in our sample takes ~ 1.4 ps (independent of photon energy and fluence in the regime considered here). This separation of time scales allows us to describe the electronic system using the electron temperature approximation.

Carrier-carrier scattering in graphene leads to the creation of secondary hot electrons that originate from the conduction band. These secondary hot electrons give a negative contribution to the THz photoconductivity, since the momentum scattering time $\tau_{\text{tr}}(\epsilon)$ increases with carrier energy ϵ [21–23]. Accounting for fast thermalization of the secondary carriers, the net change in the THz photoconductivity can be expressed as $-2aN_{\text{photon}}\mathcal{J}_{\text{el-el}}$, where N_{photon} is the absorbed photon density, and the pre-factor a is estimated in the supplementary online material (the factor of 2 accounts for two carriers (electron and hole) produced per photon). Integrating over the cascade, we obtain the conductivity at the peak:

$$\Delta\sigma \approx -2N_{\text{photon}} \int_{t_0}^{t_0 + \tau_{\text{peak}}} dt a \mathcal{J}_{\text{el-el}} = -2N_{\text{photon}} \int_0^{hf/2} d\epsilon \frac{a \mathcal{J}_{\text{el-el}}(\epsilon)}{\mathcal{J}_{\text{el-el}}(\epsilon) + \mathcal{J}_{\text{el-ph}}(\epsilon)}. \quad (1)$$

In the case that electron-electron scattering processes dominate, $\mathcal{J}_{\text{el-el}} \gg \mathcal{J}_{\text{el-ph}}$, Equation (S5) directly leads to linear scaling. In this case, since a is approximately energy independent (see supplementary online material), we have $\Delta\sigma \approx -aN_{\text{photon}}hf$, i.e. perfectly linear scaling. In a more realistic regime, when $\mathcal{J}_{\text{el-el}} \sim \mathcal{J}_{\text{el-ph}}$, the THz photoconductivity in Equation (S5) is sensitive to the branching ratio of the two processes, $\alpha(\epsilon) = \mathcal{J}_{\text{el-el}}/\mathcal{J}_{\text{el-ph}}$. Using $\mathcal{J}_{\text{el-el}}$ from electron-electron scattering events described in Ref. [24] and writing $\mathcal{J}_{\text{el-ph}} = \gamma(\epsilon - \omega_0)\Theta(\epsilon - \omega_0 - E_F)$ we obtain the branching ratios plotted in Fig. 2b. Here ω_0 is the optical phonon energy (0.2 eV), Θ is a step function and γ (in $(\text{ps})^{-1}$) is the coupling constant between electrons and optical phonons, which we use as a fitting parameter to obtain the branching ratio. Since other Auger processes like interband relaxation of carriers are blocked kinematically [25], $\mathcal{J}_{\text{el-el}}$ from impact excitation captures the relevant carrier-carrier scattering processes. Since the branching ratio has a strong energy dependence (approximately $\propto 1/\epsilon$ at high energies), we use the scaling of $\Delta\sigma$ with photon energy as a sensitive probe of the magnitude of the branching ratio. Indeed, $\Delta\sigma/N_{\text{ph}}$ from Equation (1) begins to deviate from linear scaling (with hf) significantly when the branching ratio becomes smaller than unity, $\alpha(\epsilon) < 1$.

In Fig. 2a, we compare Equation (1) for three values of the electron-phonon coupling constant γ to our observed differential transmission signal normalized by absorbed photon density (see supplementary online material). The best-fit value $\gamma \approx 4 \text{ ps}^{-1}$ corresponds to the solid curve in Fig. 2a. The branching ratio values indicate that electron-electron scattering dominates the energy relaxation cascade. For stronger electron-phonon coupling, i.e. larger values of γ , we find that $\Delta\sigma$ from Equation (1) bends down at higher energies, significantly deviating from linearity, as illustrated by the dotted curve for $\gamma = 10 \text{ ps}^{-1}$. We can exclude fits with $\gamma > 10 \text{ ps}^{-1}$ as the data clearly lie in the range $1 \text{ ps}^{-1} \lesssim \gamma \lesssim 10 \text{ ps}^{-1}$. Inspecting the branching ratios that correspond to $\gamma = 1, 4, \text{ and } 10 \text{ ps}^{-1}$ (see Fig. 2b) we conclude that the energy relaxation cascade that produces our observed $\Delta T/T_0$ have branching ratio $\alpha(\epsilon) \gtrsim 1$. Hence, electron-electron scattering dominates the energy relaxation cascade of photoexcited carriers, prevailing over electron-optical phonon scattering.

We find good agreement between our experimental observations and values predicted by the model. First of all, the branching ratio we find in Fig. 2b is in good agreement with the theoretically predicted branching ratio. Using the known value of the electron-optical phonon deformation potential [26], we compute $\gamma = 1.36 \text{ ps}^{-1}$ (see supplementary online material), which lies in the range of γ 's obtained by fitting the data. In the supplementary text we also show that the experimentally observed magnitude of the signal is in reasonable agreement with the theoretical result for a based on the effective temperature model. Furthermore, it is interesting to note that the rise time of the pump probe signal in Fig. 1b – corresponding to the time needed for the energy relaxation cascade – is longer for excitation with a higher photon energy. Although our experimental time resolution is only marginally smaller than the rise time, the variation with photon energy indicates that the observed behavior at $t \lesssim \tau_{\text{peak}}$ is not limited by time resolution. The observed dependence is in qualitative agreement with the theoretical prediction of longer cascade times at higher photon energy, where more carrier-carrier scattering events occur during the cascade [24].

Using the branching ratios plotted in Fig. 2b, we calculate the fraction of the photon energy that remains in the electronic system after the cascade (integrated e-e efficiency) as

$$\eta(\epsilon_i) = \frac{1}{\epsilon_i} \int_0^{\epsilon_i} \frac{\alpha(\epsilon)}{\alpha(\epsilon) + 1} d\epsilon \quad \epsilon_i = hf/2. \quad (2)$$

We plot $\eta(\epsilon_i)$ for $\gamma = 1 \text{ ps}^{-1} - 10 \text{ ps}^{-1}$ in Fig. 2c showing that more than 50% of the photon energy remains in the electronic system even for photoexcitation energies as high as $hf = 3 \text{ eV}$. This shows that carrier-carrier interaction in graphene is highly efficient. We note that our model may overestimate the efficiency at low energies, as close to the Fermi surface energy relaxation may depend on pathways that were not included in the model: acoustic phonons, flexural phonons and substrate surface phonons. However, since these processes only become important close to the Fermi surface we expect their impact on the total efficiency to be small.

For most applications the relevant figure of merit is the integrated efficiency η as it describes the fraction of light energy that is passed to the electronic system, where hot carriers can drive currents of optoelectronic systems. However it is also interesting to examine how many hot electrons are created from a single incident photon. Our model predicts that the number of secondary hot electrons scales approximately linearly with photon energy, $N \sim \epsilon_i/\mu$ [24]. Taking into account the extracted efficiency of 80% for excitation with 3 eV pump light, we find that 9 additional hot electrons are created, that get promoted from below to above the Fermi level in the conduction band. [24].

Our study reveals efficient carrier-carrier interaction in graphene, thereby resolving a long-standing question about the relative importance of electron-electron scattering versus emission of optical phonons in the energy relaxation cascade triggered by photoexcitation. Crucially, the transfer of energy from photoexcited carriers to electronic degrees of freedom in graphene is efficient over a wide range of frequencies (from the UV to the infrared), unlike conventional semiconductor systems where the frequency range is limited by the band gap. Furthermore, the number of secondary hot electrons is expected to be highly sensitive to the doping level [24], enabling effective manipulation of the energy cascade pathways. Thus graphene enables enhanced quantum efficiencies and tunable energy transfer over a wide spectral range.

-
- [1] Nair, R.R. et al. *Science* **320**, 1308–1308 (2008)
- [2] Kotov, V.N. et al. *Rev. Mod. Phys.* **84**, 1067–1125 (2012)
- [3] Bonaccorso, F., Sun, Z., Hasan, T. & Ferrari, A.C. *Nature Phot.* **4**, 611–622 (2010).
- [4] Winzer, T., Knorr, A. & Malić, E. *Nano Lett.* **10**, 4839–4843 (2010).
- [5] Winzer, T. & Malić, E. *Phys. Rev. B* **85**, 241404(R) (2012).
- [6] Gabor, N.M. et al. *Science* **334**, 648–652 (2011).
- [7] Song, J.C.W. et al. *Nano Lett.* **11**, 4688–4692 (2011).
- [8] Pijpers, J.J.H. et al. *Nature Phys.* **5**, 811 (2009).
- [9] Pijpers, J.J.H. et al., *J. Phys. Chem. C* **111**, 4146–4152 (2007).
- [10] Schaller, R.D. & Klimov, V.I. *Phys. Rev. Lett.* **92**, 186601 (2004)
- [11] Schaller, R.D. Agranovitch, V.M. & Klimov, V.I. *Nature Phys.* **1**, 189 (2005). **83**, 543–586 (2011).
- [12] Ulbricht, R. et al. *Rev. Mod. Phys.*
- [13] George, P.A. et al. *NanoLett.* **8**, 4248 (2008).
- [14] Strait, J.H. et al. *Nano Lett.* **11**, 4902–4906 (2011).
- [15] Winnerl, S. et al. *Phys. Rev. Lett.* **107**, 237401 (2011).
- [16] Breusing, M., Ropers, C. & Elsaesser, T. *Phys. Rev. Lett.* **102**, 086809 (2009).
- [17] Breusing, M. et al. *Phys. Rev. B* **83**, 153410 (2011).
- [18] Kampfrath, T. et al. *Phys. Rev. Lett.* **95**, 187403 (2005).
- [19] H.Y. Hwang et al. *Arxiv*: 1101.4985 (2011).
- [20] Frenzel, A.J., Private Communication (2012).
- [21] Nomura, K & MacDonald, A.H. *Phys. Rev. Lett.* **96**, 256602 (2006).
- [22] Ando, T. *J. Phys. Soc. Jpn.* **75**, 074716 (2006).
- [23] Das Sarma, S.D., Adam, S., Hwang, E.H. & Rossi, E. *Rev. Mod. Phys.* **83**, 407 (2011).
- [24] Song, J.C.W. et al. *Arxiv*: 1209.4346.
- [25] Foster, M.S. & Aleiner, I.L. *Phys. Rev. B* **79** 085415 (2009).
- [26] Bistritzer, R. & MacDonald, A.H. *Phys. Rev. Lett.* **102** 206410 (2009).
- [27] Tse, W.-K. & Das Sarma, S.D. *Phys. Rev. B* **79**, 235406 (2009).
- [28] Song, J.C.W., Reizer, M.Y. & Levitov, L.S. *Phys. Rev. Lett.* **109** 106602 (2012).
- [29] D. Grischkowsky et al. *J. Opt. Soc. Am. B* **7**, 2006–2015 (1990)
- [30] J. Horng et al. *Phys. Rev. B* **83**, 165113 (2011)
- [31] K.F. Mak, J. Shan and T.F. Heinz, *Phys. Rev. Lett.* **106**, 046401 (2011)
- [32] S. Pisana et al. *Nature Mat.* **6**, 198–201 (2007)
- [33] A. Das et al. *Nature Nanotech.* **3**, 210–215 (2008)
- [34] M. C. Nuss, and J. Orenstein, *Millimeter and Submillimeter Wave Spectroscopy of Solids*, Chp. 2, Springer-Verlag, Berlin (1998)
- [35] G. Grosso, and G. P. Parravicini, *Solid State Physics*, Academic Press (2003)
- [36] R. Bistritzer, A. H. MacDonald, *Phys. Rev. Lett.*, 102 206410 (2009)
- [37] Vasili Perebeinos, and Phaedon Avouris, *Phys. Rev. B*, **81** 195442 (2010)
- [38] W.-K. Tse, E. H. Hwang, and S. D. Das Sarma, *Appl. Phys. Lett.*, 93 023128 (2008)

II. ACKNOWLEDGEMENTS

We acknowledge financial support from an NWO Rubicon grant (KJT), the NSS program, Singapore (JS), the Office of Naval Research Grant No. N00014-09-1-0724 (LL), and Fundacio Cellex Barcelona and ERC Career integration grant GRANOP (FK).

III. FIGURES

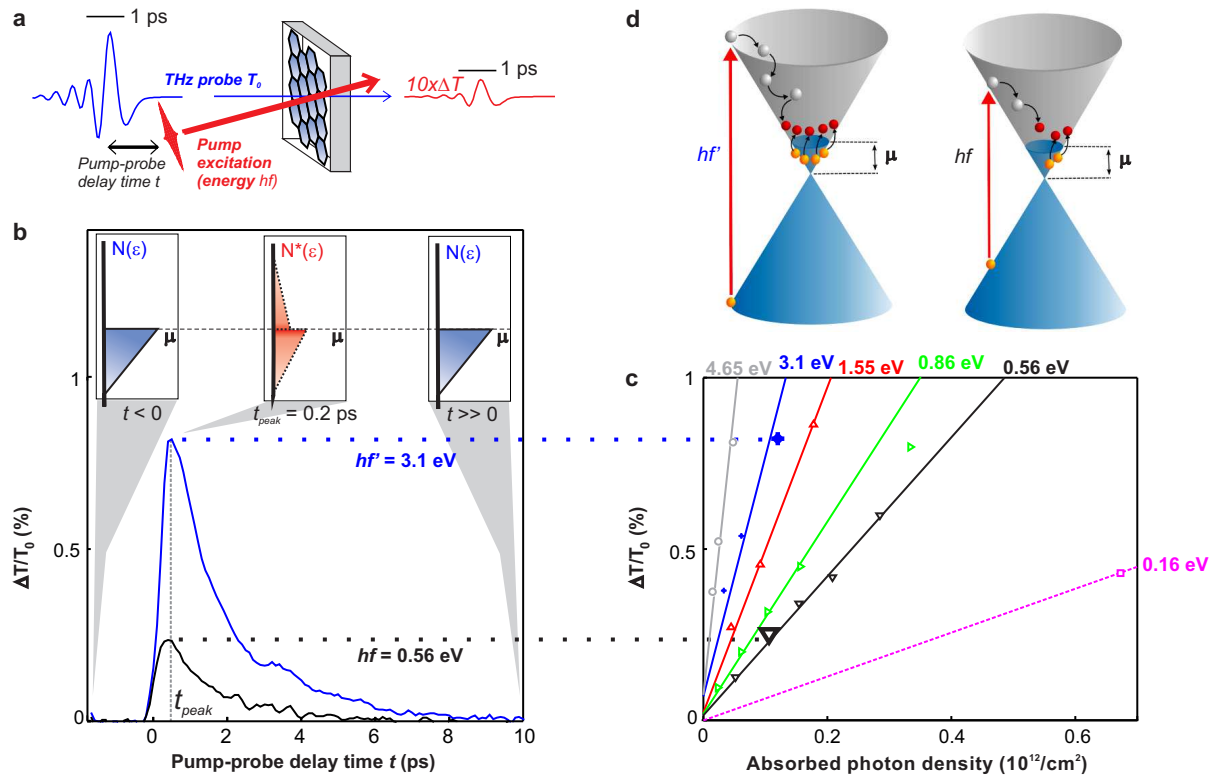


FIG. 1:

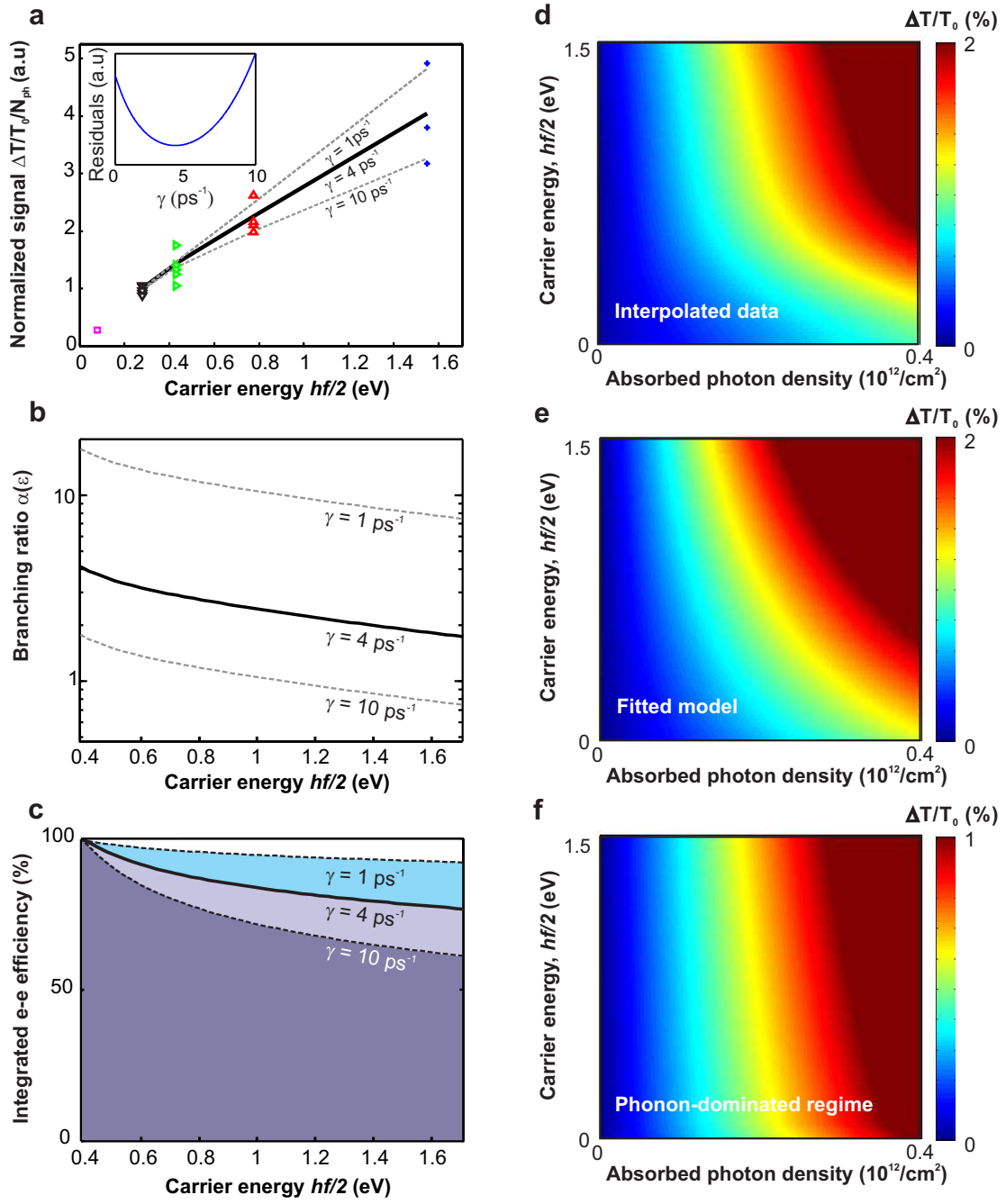


FIG. 2:

IV. FIGURE CAPTIONS

Figure 1

Experimental realization and results. **a)** Experimental observation of carrier dynamics. Photoexcitation of electron-hole pairs in graphene monolayer by a pump pulse is followed by a Terahertz probe pulse that provides a measurement of the pump-induced change in THz electric field transmission $\Delta T = T - T_0$ (red curves). The time dynamics of the photoexcited carriers is studied by varying the time delay t between the pump pulse and the probe pulse. The change in transmission ΔT , which is directly proportional to the change in THz conductivity, is used to characterize the degree to which secondary hot electrons are produced as the photoexcited electron cascades down to the Fermi level. **b)** Time resolved carrier dynamics for two different photon energies: the pump-induced change in THz transmission $\Delta T/T_0$ as a function of pump-probe delay time t for fixed absorbed photon density $N_{\text{photon}} \sim 0.1 \times 10^{12} \text{ cm}^{-2}$. The insets show a schematic representation of the carrier distribution $N(\epsilon)$ before ($t < 0$) and long after ($t \gg \tau_{\text{peak}}$) pump excitation, and the hottest carrier distribution $N^*(\epsilon)$ directly after the energy relaxation cascade ($t = \tau_{\text{peak}}$). **c)** Scaling of the differential transmission signal $\frac{\Delta T}{T_0}$ peak values, obtained from the time traces as in **b** at $t = \tau_{\text{peak}}$ for six photon energies as a function of absorbed photon density N_{photon} . The lines are linear fits to guide the eye, showing that the signal increases linearly with absorbed photon density. For a given absorbed photon density N_{photon} a higher photon energy hf leads to an increased signal, corresponding to a hotter carrier distribution. **d)** The effect of varying hf on the energy cascade illustrated for two photon energies, $hf' > hf$. Photoexcitation creates a primary electron-hole pair, and triggers a cascade of carrier-carrier scattering steps, where energy is transferred to multiple secondary hot electrons in the conduction band, generating a hot carrier distribution. The number of secondary hot electrons increases with photon energy, leading to a hotter carrier distribution and a larger observed $\frac{\Delta T}{T_0}$ signal.

Figure 2

Carrier-carrier scattering efficiency. **a)** Extraction of the branching ratio between e-e scattering and optical phonon emission from comparison of the experimental data and model: The pump-probe signal $\frac{\Delta T}{T_0}$ peak value normalized by absorbed photon density N_{photon} features approximately linear scaling with hf , indicating that electron-electron scattering dominates the energy relaxation cascade (see text). Deviation from linearity is accounted for in the model by including optical phonon emission with a coupling strength γ (see Equation (1)). The best-fit curve ($\gamma = 4 \text{ ps}^{-1}$, solid line) and the curves that marginally agree with the experimental data ($\gamma = 1 \text{ ps}^{-1}$ and $\gamma = 10 \text{ ps}^{-1}$, dashed line) are shown. The inset shows the fit residuals. **b)** The branching ratio for the carrier-carrier scattering and optical phonon emissions pathways as a function of initial carrier energy for the three coupling strengths shown in **a**. Larger-than-one values indicate that electron-electron scattering is the dominant energy-relaxation pathway. **c)** The integrated efficiency for the carrier-carrier scattering pathway as a function of carrier energy for the same three coupling strength values: best-fit (solid line), and upper and lower bounds. The estimated efficiencies are well above 50%, indicating that a large fraction of incident photon energy is transferred to the electronic system through efficient carrier-carrier scattering. **d,e,f)** “Bird’s eye view” of the differential signal vs. photon energy and absorbed photon number density for experimental data (**d**), model best-fit (**e**) and (simulated) phonon-emission-dominated cascade (**f**). For efficient carrier-carrier scattering, the differential transmission signal is expected to increase with both absorbed photon density N_{photon} and with carrier energy $hf/2$. The contour lines of constant $\frac{\Delta T}{T_0}$ as a function of N_{photon} and $hf/2$ obtained by interpolation of the data (**d**) indeed show this behavior. The good overall correspondence with the model for a best-fit γ value (**e**) further corroborates the conclusion that e-e scattering dominates the cascade. In contrast, simulation of phonon-emission dominated cascade ($\gamma = 100 \text{ ps}^{-1}$, **f**) shows significant departure from the data.

V. APPENDIX

S1. OPTICAL PUMP - TERAHERTZ PROBE TECHNIQUE

The optical pump - Terahertz probe setup is based on an ultrafast amplified laser system with a pulse duration of ~ 50 femtoseconds, a center wavelength of 800 nm and a repetition rate of 1 kHz. Part of the output is used to create the optical pump pulses and part is used to create the THz probe pulses. The optical pump pulses have a photon energy that we vary using non-linear optical conversion. To create 400 nm excitation pulses, we use frequency doubling in a β -Barium Borate (BBO) nonlinear crystal ($\theta = 29.2^\circ$, 1 mm) and for the 267 nm pulses, we use the sum frequency of 400 nm and 800 nm pulses in a second BBO crystal ($\theta = 44.3^\circ$, 0.2 mm). For the excitation pulses in the infrared, we feed the 800 nm pulses into a home-built optical parametric amplifier (OPA), which we tune to either produce signal pulses at 1400 nm or idler pulses at 2100 nm. Finally, for the 8 μm pulses, we use a AgGaS₂ nonlinear crystal ($\theta = 50^\circ$, 1.2 mm) for difference frequency mixing between 1455 nm idler pulses and 1778 nm idler pulses. The pump pulses pass through a diffuser to ensure spatially homogeneous excitation of the graphene sample and through a 500 Hz chopper so that we alternately probe the THz electric field transmission with and without photo-excitation by pump pulses, $T_0 + \Delta T$ and T_0 , respectively. We determine the pump fluence at each wavelength by measuring the transmission through five holes of different well-known sizes with a calibrated power meter. The 8 μm and 267 nm pump pulses had very low fluences and therefore did not pass through the diffuser. Excitation without diffuser could lead to an underestimation of the absorbed photon density in the case of hot spots in the beam profile and therefore these two photon energies are not taken into account for the determination of the efficiency of carrier multiplication.

The THz probe pulses are created through optical rectification in ZnTe nonlinear crystal (110 orientation, 0.5 mm) and focused on the sample. After recollecting and collimating, the THz beam is focused on a second ZnTe crystal and overlapped in time with an 800 nm sampling beam, whose polarization is rotated by the presence of the electric field of the THz beam. We then detect this polarization rotation, which is directly proportional to the electric field strength of the THz beam. By varying the time delay between the THz beam and the 800 nm sampling beam, we obtain the time evolution of the THz pulse. For the pump-probe measurements described here, we position this time delay such that we are at the peak of the THz pulse. We then change the time delay of the pump pulses with respect to the peak of the THz pulse in order to follow the temporal evolution of the THz pump-probe signal, which is proportional to the THz photoconductivity in the thin film approximation: $\Delta\sigma = -\frac{\Delta T}{T_0} \frac{n_s+1}{Z_0}$. Here $n_s = 1.95$ [29] is the refractive index of the quartz substrate and $Z_0 = 377 \Omega$ is the free space impedance. All measurements were done at room temperature. We verify the sign of the pump-probe signal by comparing measuring the signal through a silicon sample and our monolayer graphene sample sequentially without changing the chopper in Lock-in Amplifier phase settings.

S2. SAMPLE CHARACTERIZATION

The graphene samples consist of a large ($\sim 1 \text{ cm}^2$) single graphene layer that was grown by chemical vapor deposition (CVD) and subsequently transferred onto a 200 μm thick fused silica substrate (CFS-2520 from UQG Optics). To determine the intrinsic doping of the graphene layer, we performed Raman spectroscopy (see Fig. S1A). We find a G peak located at 1586 cm^{-1} corresponding to a Fermi level of $E_F = 0.17 \pm 0.05 \text{ eV}$ and thus an intrinsic doping of $n_{\text{intr}} \sim 2 \times 10^{12} \text{ carriers/cm}^{-2}$ [32, 33]. The FWHM of the 2D peak is $30 \pm 5 \text{ cm}^{-1}$, confirming that our sample is monolayer graphene. We measured the THz transmission (without optical pump excitation) and find that the graphene layer leads to a spectrally flat absorption of $\sim 5\%$ in the THz region (see Fig. S1B). Using the thin film approximation we find that this absorption corresponds to an intrinsic sheet conductivity of $\sigma_{\text{intr}} \approx \frac{T_{\text{sub}} - T_0}{T_{\text{sub}}} \frac{n_s + 1}{Z_0} = 4 \times 10^{-4} \text{ S/m}$ (or $\sim 10e^2/h$), with T_{sub} the transmission through the substrate without graphene. The (Drude) sheet conductivity in graphene is determined by the carrier density and the weighted momentum scattering time ($\langle \tau_{\text{tr}} \rangle$). We use the carrier density from the Raman measurements to extract a momentum scattering time of $\sim 20 \text{ fs}$, similar to earlier conductivity studies of large area CVD graphene [14, 30]. This shows that the extracted intrinsic carrier density is realistic and that THz radiation is an excellent probe for the free carrier conductivity. We note that the substrate thickness of 200 μm results in a small additional peak in the pump-probe delay traces at a delay time of $\sim 3 \text{ ps}$ due to reflection of the THz wave. We have confirmed that this peak is absent when using a thicker substrate.

In our measurements we measure the pump-induced change of the conductivity of the free carriers, i.e. the THz photoconductivity. In order to make quantitative comparisons between the THz photoconductivity induced by

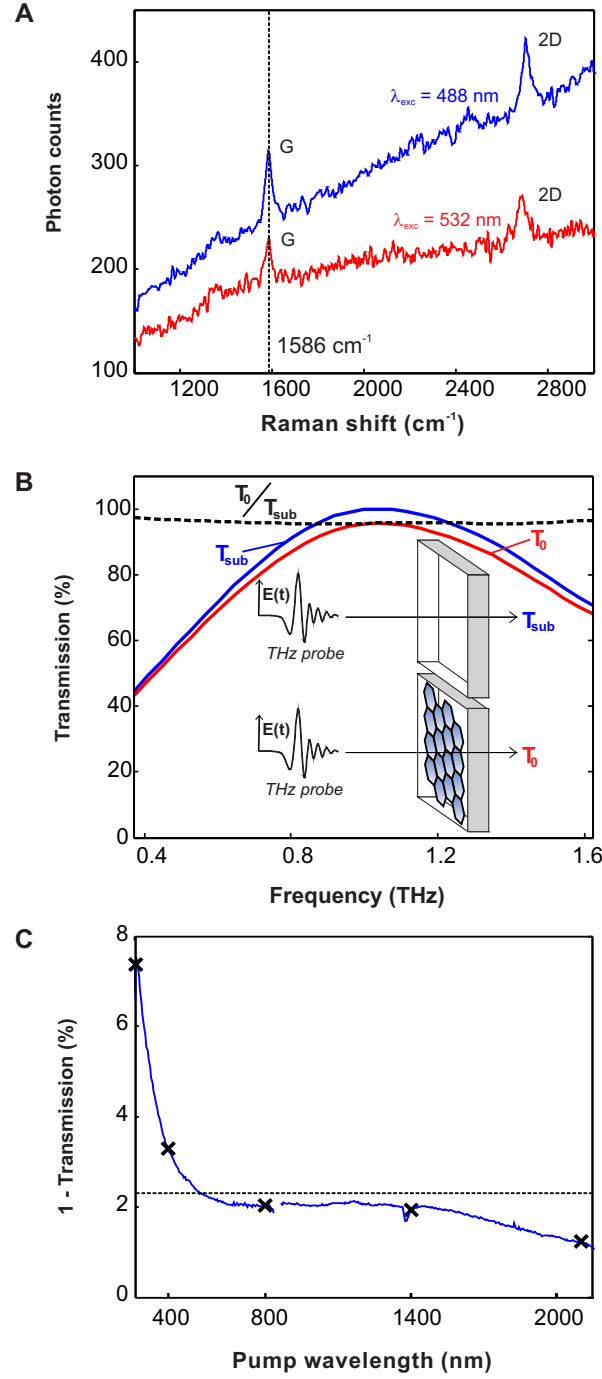


FIG. S1: *Sample characterization.* **A)** Raman spectroscopy to determine the intrinsic carrier density through substrate doping. **B)** Terahertz transmission spectrum, showing spectrally flat absorption of $\sim 5\%$, due to the conductivity of the intrinsic free carriers. **C)** Absorption spectrum to determine the absorption for the used pump wavelengths, indicated by black crosses.

photo-excitation with different photon energies, we need to accurately know the number of absorbed photons at each pump wavelength. We obtain this number through the measurement of the fluence (the energy of the pump beam per unit of area) and through the graphene absorption at each pump wavelength. We determined the graphene absorption using a standard double beam spectrometer (Perkin Elmer Lambda 950), where we placed an identical quartz substrate without graphene in the reference path. The absorption was determined from 200 nm up to $2.2 \mu\text{m}$ (see Fig. S1C), above which the substrate starts absorbing strongly. The change in reflection due to the presence of graphene is negligibly small ($<0.1\%$) [1]. We find relatively flat absorption that is slightly lower than the universal

value of 2.3% [1], down to a wavelength of ~ 500 nm and increased absorption due to excitonic effects that peak around 250 nm [31].

S3. DIFFERENTIAL TRANSMISSION, THZ CONDUCTIVITY, AND THZ PHOTOCONDUCTIVITY

The transmission, $T(\omega)$, of light at a frequency ω through a single graphene layer and substrate stack (in the thin film approximation) is related to its optical conductivity, $\sigma(\omega)$ via [14, 34]

$$\frac{T}{T_{\text{sub}}} = \left[1 + \frac{\sigma(\omega)Z_0}{n_s + 1} \right]^{-1}, \quad (\text{S1})$$

where T_{sub} is the transmission through the substrate only (no graphene), $Z_0 = \sqrt{\mu_0/\epsilon_0}$ is the impedance of free space, and n_s is the index of refraction of the substrate. Throughout this text, we only consider the *real* part of the optical conductivity which we will denote by σ . In pump-probe experiments, It is natural to consider the change in transmission that is due to the pumping of the sample. The difference between pump on and pump off transmission, $\Delta T = T - T_0$ where T_0 corresponds to the transmission with pump off, is also related to the change in optical conductivity of the graphene sample due to optical pumping. This gives

$$\frac{\Delta T}{T_0} = \frac{1 + [\sigma_0(\omega)Z_0]/[n_s + 1]}{1 + [\sigma_1(\omega)Z_0]/[n_s + 1]} - 1 \approx -\Delta\sigma(\omega)\frac{Z_0}{n_s + 1}, \quad (\text{S2})$$

where $\sigma_0(\omega)$ is the optical conductivity with pump off, $\Delta\sigma = \sigma_1(\omega) - \sigma_0(\omega)$ and in the last line we have used $[\sigma(\omega)Z_0]/[n_s + 1] \ll 1$ and expanded the denominator. σ_1 is the conductivity when the pump is on. For ω in the ranges of 1 THz this is referred to as the Terahertz conductivity and probes intra-band scattering events as $\hbar\omega \ll E_F$.

The optical conductivity depends directly on the energy-dependent carrier distribution and gives a different value according to how far away from equilibrium the carrier distribution is. To see this, we use the kinetic equation to derive the conductivity[35]

$$\partial_t n_{\mathbf{k}} + e\mathbf{E}\nabla_{\mathbf{k}}n_{\mathbf{k}} = \sum_{\mathbf{k}'} W_{\mathbf{k}',\mathbf{k}} [(1 - n_{\mathbf{k}})n_{\mathbf{k}'} - (1 - n_{\mathbf{k}'})n_{\mathbf{k}}] = \sum_{\mathbf{k}'} W_{\mathbf{k}',\mathbf{k}} (n_{\mathbf{k}'} - n_{\mathbf{k}}) \quad (\text{S3})$$

The perturbation of the non-equilibrium distribution due to an external electric field, $n_{\mathbf{k}} = \bar{n}_{\mathbf{k}} + \delta n_{\mathbf{k}}$, can be found by the relaxation time approximation where we linearize the right hand side in $\delta n_{\mathbf{k}}$ giving $\sum_{\mathbf{k}'} W_{\mathbf{k}',\mathbf{k}} (n_{\mathbf{k}'} - n_{\mathbf{k}}) \approx -\delta n_{\mathbf{k}}/\tau_{\text{tr}}(\mathbf{k})$ where $\frac{1}{\tau_{\text{tr}}(\mathbf{k})} = \sum_{\mathbf{k}'} W_{\mathbf{k}',\mathbf{k}}(1 - \cos\theta)$. At finite frequency the carrier distribution response to an AC field $\mathbf{E} \propto e^{-i\omega t}$ gives a (real part of) conductivity

$$\sigma(\omega) = - \sum_{\mathbf{k}} \frac{\tau_{\text{tr}}(\epsilon_{\mathbf{k}})}{1 + [\omega\tau_{\text{tr}}(\epsilon_{\mathbf{k}})]^2} e^2 v_{\mathbf{k}} \nabla_{\mathbf{k}} n_{\mathbf{k}} \quad (\text{S4})$$

where we have used the formula for current $\mathbf{j} = \sum_{\mathbf{k}} e v_{\mathbf{k}} \delta n_{\mathbf{k}}$ and picked out the ω response.

As described in the main text upon pumping by optical pulse, a narrow band of photo-excited carriers is created. These photo-excited carriers can relax energetically in two primary ways depicted in Fig. 1 of the main text : (i) carrier-carrier scattering with carriers in the Fermi sea or by emission of optical phonons. Both processes can lead to a change in the THz conductivity : termed THz photoconductivity. The former excites the carrier distribution about the Fermi surface leading to a hotter carrier distribution and a change in the THz conductivity. Because the transport time increases with carrier energy [21–23], the change in the real part of conductivity (measured in transmission) is negative. The latter process produces optical phonons which can act as scattering centers for carriers in the Fermi sea, increasing the resistivity of the sample.

In the following we consider both processes. Accounting for fast thermalization of the secondary carriers, the net change in the THz photoconductivity can be expressed as $-2N_{\text{photon}}(a\mathcal{J}_{\text{el-el}} + b\mathcal{J}_{\text{el-ph}})$, with the energy relaxation of the photoexcited carriers described in a general form via $d\epsilon/dt = -\mathcal{J}_{\text{el-el}}(\epsilon) - \mathcal{J}_{\text{el-ph}}(\epsilon)$, where ϵ is the photo-excited carrier energy and $\mathcal{J}_{\text{el-el}}$ and $\mathcal{J}_{\text{el-ph}}$ represent the energy relaxation rates for processes (i) and (ii). Here a is the coefficient governing the change in THz conductivity from the capturing of energy by the electronic system (see below), and b is the coefficient governing the change in THz conductivity from the emission of optical phonons that act as scattering centers (see below). As a result, the THz photoconductivity from these two processes is

$$\Delta\sigma = -2N_{\text{photon}} \int_{t_0}^{t_0+\tau_{\text{peak}}} dt (a\mathcal{J}_{\text{el-el}} + b\mathcal{J}_{\text{el-ph}}) = -2N_{\text{photon}} \int_0^{hf/2} dE \frac{a\mathcal{J}_{\text{el-el}} + b\mathcal{J}_{\text{el-ph}}}{\mathcal{J}_{\text{el-el}} + \mathcal{J}_{\text{el-ph}}}, \quad (\text{S5})$$

To get a gauge of which processes contribute most to the photoconductivity, we note that for a photon energy of $hf = 3.1$ eV, and $N_{\text{photon}} = 10^{11} \text{ cm}^{-2}$ our experiments found a transmission change of 0.75% (Fig. 1C of main text) which corresponds to a photoconductivity of $\Delta\sigma \approx -1.5e^2/h$. Using values of b , $E_F = 0.17$ eV in our samples, $\mathcal{J}_{\text{el-el}}$, and $\mathcal{J}_{\text{el-ph}}$ calculated below, we find that the optical phonon scattering contribution to photoconductivity is $\Delta\sigma_{\text{ph}} \approx -0.02e^2/h$ about 75 times smaller than what is observed. Hence, we conclude that the scattering off emitted optical phonons produce negligibly small contribution to the photoconductivity. As a result, we set $b = 0$ in our analysis of our data (see Eq. 1, Fig. 2 of main text and discussion below).

S4. ELECTRONIC TEMPERATURE MODEL FOR a

We consider the photoconductivity due to carrier-photoexcited carrier scattering. This process excites the carrier distribution about the Fermi surface. Because carrier-carrier scattering is fast on the order of 10s of fs [13, 24] - shorter than the initial rise time ~ 200 fs measured in our pump-probe experiment (see Fig. 1C of the main text) - the excited carrier distribution thermalizes quickly and can be described by an increased effective electronic temperature, T . Thermal equilibration with the lattice in graphene is slow [27, 28, 36], and in our samples takes ~ 1.4 ps (see Fig. 1B of main text). This separation of time scales allows us to treat the electronic system as out of equilibrium with the lattice.

In the degenerate limit, $E_F \gg k_B T$, we can use the Sommerfeld expansion in Eq. S4 giving a (real part of) THz conductivity

$$\sigma(\omega) \approx \sigma(\omega)_{T=0} + \frac{\pi^2}{6} \nu(E_F) k_B^2 T^2 \frac{\partial^2 F(\epsilon)}{\partial \epsilon^2} \Big|_{\epsilon=E_F}, \quad F(\epsilon) = e^2 v^2 \frac{\tau_{\text{tr}}(\epsilon)}{1 + \omega^2 [\tau_{\text{tr}}(\epsilon)]^2} \quad (\text{S6})$$

where E_F is the Fermi energy, $\nu(\epsilon)$ is the total density of states in graphene, and v is the Fermi velocity. We have kept the total carrier density, n , constant by accounting for changes in chemical potential as a function of temperature $\mu \approx E_F - \frac{\pi^2}{6} k_B^2 T^2 / E_F$. Here we have neglected the temperature dependence of the transport time, $\tau_{\text{tr}}(\epsilon)$, since we estimate that $k_B \Delta T < E_F$. We note that these, in principle, can provide additional terms to Eq. S6 and can be included in a more sophisticated analysis.

Therefore, the hot carrier contribution to the photoconductivity arising from an increase in temperature of the carrier-distribution, $\Delta\sigma_{\text{el}} = \sigma_1 - \sigma_0$ is

$$\Delta\sigma_{\text{el}} = \left(k_B^2 T_1^2 - k_B^2 T_0^2 \right) \frac{\pi^2}{6} \nu(E_F) \frac{\partial^2 F(\epsilon)}{\partial \epsilon^2} \Big|_{\epsilon=E_F} \quad (\text{S7})$$

where 1, 0 subscripts indicate pump on and off respectively.

We note parenthetically that the differential transmission in our set-up is related to the the photoconductivity above but with a sign that is opposite to $\frac{\partial^2 F(\epsilon)}{\partial \epsilon^2}$. For graphene, $\frac{\partial^2 F(\epsilon)}{\partial \epsilon^2} < 0$ for small probing frequencies $\omega \sim \text{THz}$ because $\tau_{\text{tr}} \propto \epsilon$ [21–23]. As a result, our observed positive differential transmission (or equivalently negative photoconductivity) is consistent with a hotter carrier distribution. On the other hand, if carrier density had increased (for example, by exciting electrons from the valence band), this would have resulted in a positive photoconductivity (which we did not observe).

We can relate $\Delta\sigma_{\text{el}}$ to the change in heat in the system. In the degenerate limit, the electronic heat capacity is $C = \alpha T$ where $\alpha = \frac{\pi^2}{3} \nu(E_F) k_B^2$. Hence, the photoconductivity is

$$\Delta\sigma_{\text{el}} = \frac{k_B^2 \Delta Q}{\alpha} \frac{\pi^2}{3} \nu(E_F) \frac{\partial^2 F(\epsilon)}{\partial \epsilon^2}, \quad \Delta Q = \frac{\alpha}{2} (T_1^2 - T_0^2). \quad (\text{S8})$$

where $\Delta Q = Q_1 - Q_0$. This means that $\Delta\sigma_{\text{el}}$ is a direct measure of the amount of heat captured by the electronic system. Since the amount of heat absorbed by the carriers in the Fermi sea comes directly from the energy-loss of the photo-excited carrier, the rate of heat entering the Fermi sea is

$$\frac{d\Delta Q}{dt} = \mathcal{J}_{\text{el-el}} N_{\text{photon}} \quad (\text{S9})$$

where $-\mathcal{J}_{\text{el-el}}$ is the energy-loss rate of the photo-excited carrier due to carrier-carrier scattering between the photo-excited carrier and the carriers in the Fermi sea and N_{photon} is the absorbed photon density (ie. density of initial photo-excited carriers). We have neglected thermal equilibration with the lattice as the time scales for cooling to the lattice ~ 2 ps are far longer than the time scales of energy-loss of the photo-excited carrier ~ 40 fs [13, 24].

As a result, the photoconductivity from the relaxation of the photo-excited carriers produces the first term in Eq. S5 with

$$a = -\frac{\partial^2 F(\epsilon)}{\partial \epsilon^2} \quad (\text{S10})$$

Here a is a positive quantity. As seen above, the photo-conductivity (and hence the differential transmission) is directly sensitive to the energy relaxation dynamics of the photo-excited carrier and $\Delta\sigma_{\text{el}}$ a unique probe of the amount of energy that gets captured by the electronic system.

In the following, we estimate a from this model. Since conductivity in graphene for high doping depends linearly on density $n \propto \mu^2$ [23], the einstein relation, $\sigma = e^2 v^2 \nu(\mu) \tau(\mu) / 2$ tells us that $\tau(\epsilon) = \alpha \epsilon$, where α is a proportionality constant. The factor of 2 in the einstein relation comes from dimensionality. This is consistent with carriers scattering off Coulomb disorder in graphene [21–23]. We measured a transport time at $\epsilon = \mu$ of 20 fs (see above section) and a doping corresponding to $E_F = 170$ meV (see Raman Spectroscopy above). Therefore, we infer that in our sample $\alpha \approx 117$ fs eV $^{-1}$.

Differentiating F , and using $E_F = 0.17$ eV and a typical THz frequency that was used $\omega = 2\pi$ THz (corresponding to $f \sim 1$ THz) we obtain

$$a \approx 2.68 \times 10^{-12} \times \frac{e^2}{h} \text{cm}^2 \text{eV}^{-1} \quad (\text{S11})$$

This value for a gives a photoconductivity of $\Delta\sigma = -0.83e^2/h$ for a photon energy of 3.1 eV and absorbed photon density of $N_{\text{photon}} = 10^{11} \text{cm}^{-2}$, using the theoretical values of $\mathcal{J}_{\text{el-el}}$ and $\mathcal{J}_{\text{el-ph}}$ obtained below. Experimentally, we measure a differential transmission signal of $\Delta T/T_0 \sim 0.75\%$ for these conditions, which corresponds to $\Delta\sigma = -1.5e^2/h$, in very reasonable agreement with the theoretical result. A comparison of a with b (estimated below) yields $a/b \approx 5$ for photoexcited carrier energy of $\epsilon = 1$ eV and $\mu = 0.17$ eV.

S5. OPTICAL PHONON SCATTERING CONTRIBUTION TO PHOTOCONDUCTIVITY, b

We now consider the contribution to photoconductivity that comes from the emission of optical phonons. Optical phonons can act as scattering centers for carriers in the Fermi sea and alter the mobility of the graphene sample. Hence, a larger population of optical phonons increases the resistivity of the sample, $\Delta\rho_{\text{ph}}$, and can lead to a negative photoconductivity, $\Delta\sigma_{\text{ph}} = -\sigma_0^2 \Delta\rho_{\text{ph}}$. Here, σ_0 is the conductivity without pump excitation. In particular, the optical phonon limited resistivity is [37]

$$\Delta\rho_{\text{ph}} = \frac{2\pi D_{\text{op}}^2 \hbar N(\omega_0)}{e^2 \rho_m v^2 \omega_0} \quad (\text{S12})$$

where D_{op} is an effective electron-optical phonon coupling constant [37], ρ_m is the mass density of graphene, ω_0 is the optical phonon energy of graphene and $N(\omega_0)$ is the occupancy of optical phonons in graphene.

To estimate the occupancy $N(\omega_0)$ we note that the optical phonons that are emitted from the energy-relaxation of the photo-excited carrier similarly only have momenta $< \epsilon/(\hbar v)$ where ϵ is the energy of the photo-excited carrier. Hence, the (conditional) probability density, p , of emission of an optical phonon with wavevector \mathbf{q} given that an optical phonon was emitted by the energy relaxation of a high energy photo-excited carrier with wavevector \mathbf{k} is

$$dp = \frac{d\theta}{\pi} (1 - \cos\theta) = \frac{1}{\pi} \frac{1}{2|\mathbf{k}|} \sqrt{\frac{2|\mathbf{k}| - |\mathbf{q}|}{2|\mathbf{k}| + |\mathbf{q}|}} dq, \quad |\mathbf{q}| = 2|\mathbf{k}|\cos\theta \quad (\text{S13})$$

where θ is the angle between \mathbf{q} and $-\mathbf{k}$, and the photo-excited carrier's energy is $\epsilon = v\hbar|\mathbf{k}|$. Here we have used the factor $1 - \cos\theta$ to account for the coherence factor in the scattering matrix element. Since optical phonon scattering with carriers in the Fermi sea is mainly limited k_F far smaller than the Brillouin zone we are interested in the fraction of emitted optical phonons that lie within the circle of radius $2k_F$. The fraction of optical phonons emitted that lie within the circle of radius $2k_F$ is

$$p(|\mathbf{q}| < 2k_F) = \int_0^{2k_F} \frac{1}{\pi} \frac{1}{2|\mathbf{k}|} \sqrt{\frac{2|\mathbf{k}| - |\mathbf{q}|}{2|\mathbf{k}| + |\mathbf{q}|}} dq \approx \frac{1}{\pi} \frac{k_F}{|\mathbf{k}|} \quad (\text{S14})$$

As a result over the course of the relaxation of photo-excited carriers, the number density of optical phonons emitted within this circle of radius $2k_F$, is

$$\sum_{|\mathbf{q}| < 2k_F} N(|\mathbf{q}|) = N_{\text{photon}} \int \frac{\mathcal{J}_{\text{el-ph}}/\omega_0}{\mathcal{J}_{\text{el-ph}} + \mathcal{J}_{\text{el-el}}} \times \frac{1}{\pi} \frac{k_F}{|\mathbf{k}|} d\epsilon \quad (\text{S15})$$

where $N(|\mathbf{q}|)$ is the occupancy of optical phonons emitted. On average, each optical phonon in this circle of radius $2k_F$ contributes the same amount to the transport scattering rate between optical phonons and carriers in the Fermi surface. Hence, the average occupancy within this circle, $N_{\text{av}}^{|\mathbf{q}| < 2k_F} = [\sum_{|\mathbf{q}| < 2k_F} N(|\mathbf{q}|)] / (\sum_{|\mathbf{q}| < 2k_F} 1)$, allows us to estimate the change in resistivity coming from these optical phonons via Eq. S12. Therefore, noting that $\sum_{|\mathbf{q}| < 2k_F} 1 = \frac{\pi(2k_F)^2}{(2\pi)^2} = k_F^2/\pi$ and using Eq. S15 and Eq. S12, we find that emission of optical phonons contributes a photoconductivity described by the second term of Eq. S5 with

$$b = \frac{2\pi\sigma_0^2\hbar^2 D_{\text{op}}^2}{e^2\rho_m v\omega_0^2 k_F \epsilon} \quad (\text{S16})$$

We can estimate the value of b . Taking $D_{\text{op}} = 22.4 \text{ eV \AA}^{-1}$ [37], $\rho_m = 7.6 \times 10^{-11} \text{ kg cm}^{-2}$, $\omega_0 = 0.2 \text{ eV}$, and $\mu = 0.17 \text{ eV}$ we obtain

$$b \approx \frac{5.74 \times 10^{-13}}{(\mu [\text{eV}]/0.2) \times (\epsilon [\text{eV}])} \times \frac{e^2}{h} \text{ cm}^2 \text{ eV}^{-1}, \quad (\text{S17})$$

where we have used the measured conductivity $\sigma_0 \approx 10(e^2/h)$ (see section S2).

This value for b gives a photoconductivity of $\Delta\sigma = -0.02e^2/h$ for a photon energy of 3.1 eV and absorbed photon density of $N_{\text{photon}} = 10^{11} \text{ cm}^{-2}$. Experimentally, we found $\Delta\sigma = -1.5e^2/h$, which is significantly higher than the signal due to phonon emission only. We showed in Section S4 that the signal due to hot carriers is much larger and closer to the experimentally observed photoconductivity signal.

S6. ENERGY-RELAXATION OF PHOTO-EXCITED CARRIERS, $-\mathcal{J}$

The energy relaxation of a photo-excited carrier occurs via two processes: (i) scattering between the photo-excited carrier and the carriers in the Fermi sea (see Fig. 1B main text) allows the energy to be transferred to the Fermi sea to create a hot carrier distribution, and (ii) the emission of optical phonons. Because of the large number of carriers in doped graphene, the former process can be very efficient [24].

Additionally, the energy relaxation via this channel occurs in relatively small steps of order μ the energy relaxation rate from impact excitation events, $\mathcal{J}_{\text{el-el}}$ [24], is

$$\mathcal{J}_{\text{el-el}}(\epsilon) = (\mu[\text{eV}])^2 \xi(\epsilon/\mu) \text{ eV/ps} \quad (\text{S18})$$

where $\xi(\epsilon, \mu)$ is plotted in Fig. S2 using a numerical integration detailed in Ref. [24] (starred points in Fig. S2). We subsequently used a 4th order polynomial to interpolate between the points (dashed line in Fig. S2). For our doping, $\mu = 0.17 \text{ eV}$ we find an efficient relaxation rate that for typical carrier energies are a couple of eV/ps indicating that the relaxation of photoexcited carriers with typical energy of $\epsilon = 1 \text{ eV}$ via $\mathcal{J}_{\text{el-el}}$ occurs with a few hundred femtoseconds. This is consistent with our experimental observation of a rise time of around $\tau_{\text{peak}} \sim 200 \text{ fs}$ (see main text Fig. 1).

An alternative channel for energy relaxation of the photo-excited carrier occurs through the emission of optical phonons and gives an energy relaxation rate of $-\mathcal{J}_{\text{el-ph}}$. The transition rate of this process [38] can be described by Fermi's golden rule

$$W_{\mathbf{k}', \mathbf{k}}^{\text{el-ph}} = \frac{2\pi N}{\hbar} \sum_{\mathbf{q}} |M(\mathbf{k}', \mathbf{k})|^2 \delta(\Delta\epsilon_{\mathbf{k}', \mathbf{k}} + \omega_{\mathbf{q}}) \delta_{\mathbf{k}', \mathbf{k}+\mathbf{q}} (N(\omega_{\mathbf{q}}) + 1) \quad (\text{S19})$$

where $\Delta\epsilon_{\mathbf{k}', \mathbf{k}} = \epsilon_{\mathbf{k}'} - \epsilon_{\mathbf{k}}$, $\omega_{\mathbf{q}} = \omega_0 = 200 \text{ meV}$ is the optical phonon dispersion relation, and $N(\omega_{\mathbf{q}})$ is a Bose function. Here \mathbf{k} is the initial momentum of the photo-excited electron, \mathbf{k}' is the momentum it gets scattered into, and \mathbf{q} is the momentum of the optical phonon. The electron-phonon matrix element $M(\mathbf{k}', \mathbf{k})$ [36] is

$$|M(\mathbf{k}', \mathbf{k})|^2 = g_0^2 F_{\mathbf{k}, \mathbf{k}'}, \quad g_0 = \frac{2\hbar^2 v}{\sqrt{2\rho_m \omega_0 a^4}} \quad (\text{S20})$$

where $F_{\mathbf{k}, \mathbf{k}'}$ is the coherence factor for graphene, g_0 is the electron-optical phonon coupling constant, a is the distance between nearest neighbor carbon atoms, and ρ_m is the mass density of graphene. The energy-loss rate of the photo-excited carrier at energy ϵ due to the emission of an optical phonon is

$$\mathcal{J}_{\text{el-ph}}(\epsilon) = \sum_{\mathbf{k}'} W_{\mathbf{k}', \mathbf{k}}^{\text{el-ph}}(\epsilon'_k - \epsilon) [1 - f(\epsilon_{\mathbf{k}'})] \quad (\text{S21})$$

Integrating over \mathbf{q} and \mathbf{k}' we obtain

$$\mathcal{J}_{\text{el-ph}}(\epsilon) = \frac{\pi N}{\hbar} \omega_0 g_0^2 [1 - f(\epsilon - \omega_0)] (N(\omega_0) + 1) \nu(\epsilon - \omega_0) = \gamma(\epsilon - \omega_0) \Theta(\epsilon - E_F - \omega_0), \quad (\text{S22})$$

where $\nu(\epsilon) = \epsilon / (2\pi v^2 \hbar^2)$ is the electron density of states in graphene and we have approximated $(N(\omega_0) + 1) \approx 1$ and $1 - f(\epsilon - \omega_0) \approx \Theta(\epsilon - \omega_0 - E_F)$. γ is a constant determined by the electron-optical phonon coupling. Hence, $\mathcal{J}_{\text{el-ph}}(\epsilon)$ varies linearly with the photo-excited carrier energy $\epsilon > \omega_0$ and vanishes for $\epsilon < \omega_0$. Because the electron-phonon coupling with optical phonon is a constant, this result is to be expected from the increased phase space to scatter into at higher photo-excited carrier energy.

Using $\rho_m = 7.6 \times 10^{-11} \text{ kg cm}^{-2}$ and $a = 1.42 \text{ \AA}$ in Eq. S20 above yields $\gamma \approx 1.36 \text{ ps}^{-1}$.

S7. COMPARISON OF DATA WITH MODEL

These theoretical results for $\mathcal{J}_{\text{el-el}}$ and $\mathcal{J}_{\text{el-ph}}$ lead to a branching ratio between electron-electron scattering and electron-optical phonon scattering that we wish to compare to the experimental data. Therefore we take the experimental results for the signal normalized by absorbed photon density (Fig. 2A of the main text), which is directly proportional to $-\frac{\Delta\sigma}{N_{\text{ph}}}$, and compare these with the model through Eq. 1 of the main text. We fix $\mathcal{J}_{\text{el-el}}$ to the theoretical result and use $\mathcal{J}_{\text{el-ph}} = \gamma \Theta(\epsilon - E_F - \omega_0)$, where we use the electron-phonon coupling constant γ as the parameter that determines the experimental branching ratio. The parameter γ reflects how $-\frac{\Delta\sigma}{N_{\text{ph}}}$ depends on carrier energy (or hf): A low value of γ corresponds to an energy cascade that is dominated by el-el scattering and results in linear scaling with carrier energy, whereas a high value corresponds to el-ph dominating, which leads to the signal bending down; large γ leads to a non-linearity in $\Delta\sigma$ setting in at a low carrier energy.

We repeat the fit routine for a range of values for γ and include one fit parameter that determines the amplitude of the signal, thus serving as a mere scaling factor. In Fig. 2A we use the amplitude obtained from the best fit for all three curves, such that all curves for different γ pass through the same data point at low excitation energy (0.56 eV). We do not include the lowest (0.16 eV) and highest (4.65 eV) photon energies. In the former, the model does not cover this region and the absorbed fluence is not known very precisely. In the latter, the diffuser could not be used, which leads to possible over-estimation of the absorbed photon density (in case of hot spots in the beam profile). The fit results for $\gamma = 1, 4$ and 10 ps^{-1} are shown in Fig. 2A of the main text. Here we show the residuals (squared difference between experimental data points and model) for a range of γ 's, clearly showing a minimum around 4 ps^{-1} and strong deviation especially at large values of γ (see Fig. S2 B). This clearly shows that our data is incompatible with a phonon-dominated energy cascade. The best fitting value is somewhat larger than the theoretically obtained one (1.36 ps^{-1}), but the theoretical value still lies well within reach of the experimental data. It is also conceivable that the data leads to an overestimation of γ (and thus an underestimation of the contribution of el-el scattering) due to a nonlinear (saturation) response of the signal at high photon fluences and high photon energy. This means that we extract a conservative branching ratio.

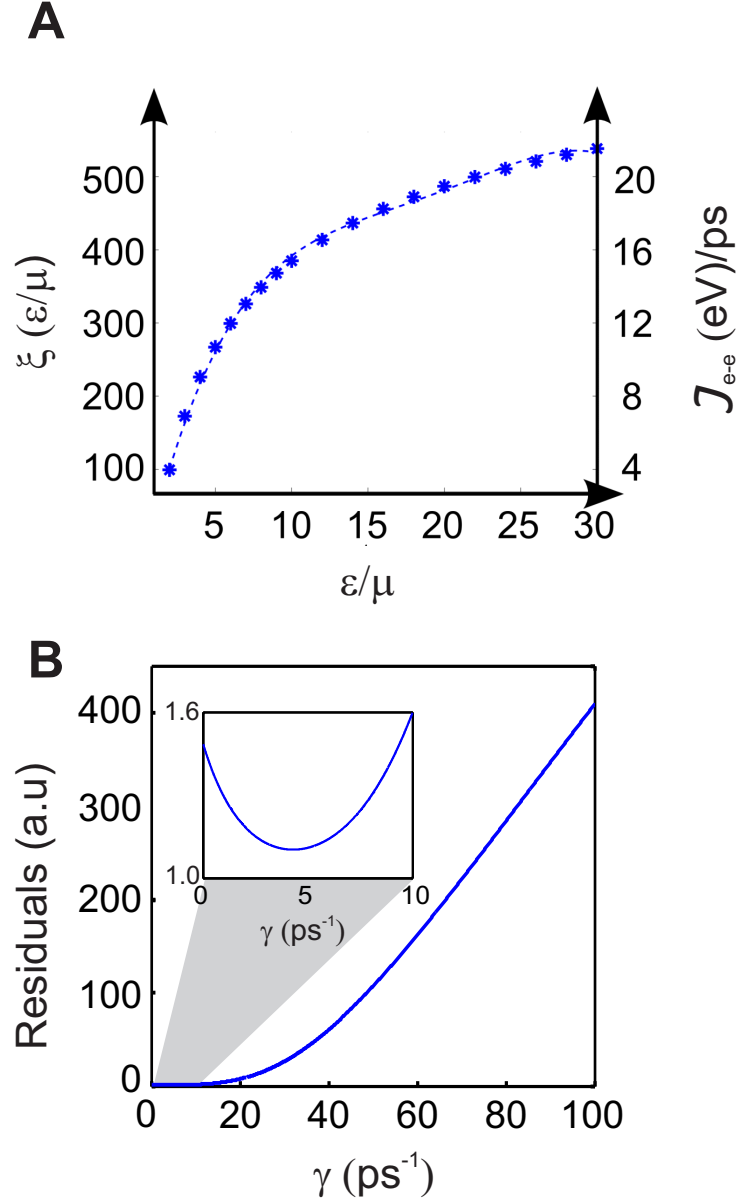


FIG. S2: **A**) (Left ordinate) Starred points denote numerical evaluation of scaling function $\xi(\epsilon/\mu)$ using Ref. [24]. Dashed lines are a 4th order polynomial fit of the numerical evaluation within this range: $\xi(x) = -3.1081 \times 10^{-3}x^4 + 0.24031x^3 - 6.8417x^2 + 92.622x - 59.383$ where $x = \epsilon/\mu$. (Right ordinate) Magnitude of \mathcal{J}_{el-el} for $\mu = 0.2$ eV using Eq. S18. **B**) The squared residuals as a function of γ , obtained by fitting the theoretical results for $\frac{-\Delta\sigma}{N_{ph}}(\epsilon)$ to the experimentally obtained $\frac{\Delta T}{T_0 N_{ph}}(\epsilon) \propto -\frac{\Delta\sigma}{N_{ph}}(\epsilon)$. The fit is done for a range of values for γ , which reflects the branching ratio, and with one free fitting parameter that is just a scaling factor. The best fit is obtained for $\gamma = 4$ ps⁻¹, and the residuals increase strongly for large values of γ .